Formation and Characterization of Nano- and Microstructured Twinned Cubic Boron Nitride

Journal:	*Physical Chemistry Chemical Physics*
Manuscript ID	CP-ART-07-2018-004592.R1
Article Type:	Paper
Date Submitted by the Author:	10-Sep-2018
Complete List of Authors:	Bhaumik, Anagh; North Carolina State University, Department of Materials Science and Engineering Narayan, Jagdish; North Carolina State University , Materials Science and Engineering

Formation and Characterization of Nano- and Microstructured Twinned Cubic Boron Nitride

Anagh Bhaumik[1], Jagdish Narayan[1]*

[1]Department of Materials Science and Engineering, Centennial Campus

North Carolina State University, Raleigh, NC 27695-7907, USA

*Correspondence to: narayan@ncsu.edu

Abstract

Nano- and microstructures of phase-pure cubic boron nitride (c-BN) are synthesized by employing nanosecond pulsed laser annealing technique at room temperature and atmospheric pressure. In the highly non-equilibrium synthesis process, nanocrystalline h-BN is directly converted into phase-pure twinned c-BN from a highly undercooled melt state of BN. By changing the nucleation and growth rates, we have synthesized a wide range of sizes (90 nm to 25 μm) of c-BN. The electron diffraction patterns indicate the formation of twinned c-BN with $[1\bar{1}1]$ as the twin axis. The twinning density in c-BN can be controlled by the degree of undercooling and quenching rate. The formation of twins predominantly occurs prior to formation of amorphous quenched BN (Q-BN). Therefore, the defect density in nano c-BN formed at higher undercooling is considerably larger than that in micro c-BN, which is formed at lower undercooling. The temperature-dependent Raman studies indicate a considerable blue-shift of ~6 cm^{-1} with decrease in temperature from 300 to 78 K in nano c-BN as compared to micro c-BN. The size-effects of c-BN crystals in Raman spectra are modeled using the spatial correlation

theory, which can be used to calculate the correlation length and twin density in c-BN. It is also found that the Raman blue-shift in nano c-BN is caused by the anharmonic effects and the decrease in Raman linewidth with decreasing temperature (300 to 78 K) is caused by three- and four-phonon decay processes. The bonding characteristics and crystalline nature of the synthesized c-BN are also demonstrated by using electron energy-loss spectroscopy and electron backscatter diffraction, respectively. We envisage that the controlled growth of phase-pure nano and microstructures of twinned c-BN and their temperature-dependent Raman-active vibrational mode studies will have a tremendous impact on low-temperature solid-state electrical and mechanical devices.

1. Introduction:

Diamond and c-BN (space group= Fd3m) being the first and the second hardest materials known have excited the researchers from their inception and have generated tremendous scientific and technological interests.[1-3] Besides hardness, diamond and c-BN have many other desirable properties, making them ideal materials for high-power, high-frequency, and radiation-hardened devices. Diamond and c-BN complement each other in view of much higher temperature stability and oxidation resistance of c-BN compared to diamond. Unlike diamond, c-BN is chemically inert and thermally stable to ferrous materials at high temperature.[4] Doping of diamond structures (*n*-type) for transistor applications is difficult and can be overcome by c-BN, which can be doped to form *p* and *n*-type semiconductors.[5] The properties of c-BN include: structure stability over a wide range of temperature (1200 K)[6] and pressure (4 GPa), extreme hardness (48 GPa), chemical inertness, high thermal conductivity (740 $Wm^{-1}K^{-1}$) and melting point (3246 K), large optical band gap (6.4 eV), *etc.*[1,7] These properties render c-BN to be used widely as pressure sensors, tools for high-speed machining, microelectronic devices, protective coatings, *etc.*[1] Since diamond and c-BN are metastable materials at ambient temperatures and pressures, they have been synthesized at high-temperature and pressure in limited quantities in bulk form. To address thin film synthesis, diamond has been synthesized by chemical vapor deposition (CVD) at high temperatures under corrosive atmospheres. The formation of epitaxial diamond has been extremely challenging due to the formation of interfacial soft amorphous carbon and disordered graphite.[8] The c-BN thin film synthesis is more challenging, as CVD methods are not well established and physical vapor deposition (PVD) methods based upon energetic nitrogen ions have led to less than 85% phase-pure c-BN.[9-11] These processes render a soft interfacial layer (of h-BN), thereby reducing adhesion and thwarting the usage of c-BN in mechanical

3

moving parts, biomedical and electronic devices. Other methods of processing of nano and micro

c-BN rely on the direct conversion of h-BN to c-BN at high temperature (1773 K) and pressure

(8 GPa) in the presence of a catalyst or solvent.[12,13] The energetic ion bombardment synthesis of

c-BN causes structural damage and stress accumulation, thereby adversely affecting the

properties of the synthesized c-BN.[14] It should also be noted that for high-speed c-BN based

electronic devices, epitaxially grown single crystalline c-BN is crucial.[9,15] Nanoscale materials

have better physical and mechanical properties than their bulk counterparts and are now being

sought after for high-speed electrical and mechanical devices.[16-18] The nanostructures of wide

band gap semiconductors such as diamond, AlN, Q-carbon, and c-BN have negative electron

affinity, thereby rendering them promising candidates for electron emission devices.[19,20] It

should also be mentioned that the twinning in diamond and c-BN leads to ultrahigh hardness and

toughness through the Hall-Petch effect, where twins block the motion of dislocations.[21]

Therefore, there is a continuous drive to synthesize nano and microstructures of twinned c-BN in

a controlled way from h-BN at room-temperature and atmospheric pressure.

Due to the high activation barrier, the pressure required for the direct phase

transformation of h-BN to c-BN far exceeds the equilibrium pressure (at 300 K). It is well known

that formation of the liquid phase of BN will drastically reduce the activation barrier [22] and will

facilitate the direct conversion of soft h-BN to extremely hard c-BN phase. Therefore, highly

non-equilibrium techniques should be adopted to synthesize phase pure c-BN. Recently, we

reported a major breakthrough in synthesis and processing of diamond by direct conversion of

amorphous carbon into diamond and Q-carbon at ambient temperature and atmospheric pressure

in air.[23,24] In this discovery, phase-pure c-BN and new amorphous phase, Q-BN[25] are formed by

nanosecond laser melting of BN and quenching subsequently to form these phases by controlling

the undercooling. By controlling the undercooling, we are able to form nano c-BN to micro c-BN and Q-BN at a higher undercooling. In addition, nanoneedles, microneedles, large-size grits, and thin films can be formed over a large area. The formation of twinning in c-BN is controlled by the quenching rates from the BN melt. Twinning in c-BN can be used to enhance hardness further *via* restricting the motion of dislocations and obtaining Hall-Petch enhancement in hardness from the spacing between the twins.[16]

In the present research, the emphasis is on the synthesis of phase-pure nano- and micro c-BN with variable twin content. The low-temperature characterization of Raman-active vibrational modes of nano-and micro c-BN is carried out to study the details of bonding characteristics. The bulk nucleation results in random c-BN, whereas interfacial growth can lead to aligned, textured, and epitaxial growth by domain matching epitaxy.[26] When c-BN is epitaxially aligned with the substrate (*c*-sapphire) useful structures for electronic devices are formed. Low-temperature (cryogenic) aspects of nano and microstructures of c-BN have not been studied as compared to high temperature and pressure conditions. Cryogenic operations (of materials) can offer certain advantages including higher operational speeds, shorter signal transmission times, lower power dissipation, improved digital and analog circuit performance (increased signal/noise ratio), *etc*. Currently, there is an urgent push for high-power, high-frequency, and high-speed radiation hardened devices, which can be addressed by c-BN nano and microstructures. Twinning needs to be minimized for electronic devices, but it improves mechanical properties by enhancing hardness as well as toughness. These nano-and microstructured materials have been characterized using various state-of-the-art techniques: temperature-dependent micro-Raman spectroscopy (300 to 78 K), high-resolution scanning electron microscopy (SEM), high-resolution transmission electron microscopy (TEM), selected

area electron diffraction (SAED), electron energy-loss spectroscopy (EELS), and electron backscatter diffraction (EBSD) for structure-property correlations and their impact on novel applications.

2. Experimental:

Pulsed laser ablation of h-BN in a laser MBE chamber was performed to deposit nanocrystalline h-BN with thicknesses ranging from 50-500 nm onto *c*-sapphire substrates at room temperature. The substrates were cleaned in acetone vapor followed by ultrasound sonication in methanol and drying (the substrates) in nitrogen. The thickness of as-deposited h-BN is varied by the number of laser shots (1 laser shot~1Å). Thicker h-BN films are used for the formation of micro and large-area c-BN after the pulsed laser annealing process, whereas thinner films are used for the formation of nano- c-BN (after PLA). The large density of grain boundaries in nanocrystalline h-BN (grain size~25 nm) facilitates melting of h-BN during the pulsed laser annealing process (due to enhanced laser - h-BN coupling). The PLD was performed in a laser MBE chamber which is maintained at a base pressure of 3×10^{-8} Torr. This base pressure is achieved by using a roughing (dry) pump in conjunction with a turbo mechanical and cryo pump. ArF excimer laser (pulse duration = 20 ns, wavelength = 193 nm, energy density = 3.0-3.5 Jcm^{-2}) is used for the deposition of nanocrystalline h-BN thin films. The laser was operated at a constant high-voltage mode (22 kV) and 10 Hz (10 laser shots per second) repetition rate during the PLD process. Therefore, for deposition of 5000 Å thick nanocrystalline h-BN onto *c*-sapphire, ~9 minutes of PLD was required. The size of laser spot on the h-BN target during the deposition was 0.06 cm^{2}, which translates into an energy density of ~3.0-3.5 Jcm^{-2}, required for laser-assisted ablation of h-BN target. Prior to the start of the deposition, pre-ablation of the target (200 laser shots at 10 Hz repetition rate) was performed. Since PLD is a highly non-equilibrium technique (due to the

forward-directed nature of the laser plume), the stoichiometry of the target is preserved on the film. After PLD, the films were irradiated (for PLA) using pulsed ArF laser having energy densities of 0.6 Jcm^{-2} to 1.0 Jcm^{-2} at room temperature and atmospheric pressure. Only one laser pulse of the nanosecond laser (ArF) is required to convert nanocrystalline h-BN into phase-pure nano c-BN structures (and amorphous quenched-BN). Multiple laser shots (up to 3) are required to grow the c-BN nano nuclei present in the amorphous Q-BN structure to micro and large-area c-BN. PLA is also a highly non-equilibrium technique due to its ultrafast nature of melting and subsequent quenching (of the laser annealed thin film). The PLA process is completed in less than 200 ns. The PLA process melts and subsequently quenches the super undercooled state of BN thereby forming nano and microstructures of c-BN. Increasing the undercooling leads to the formation of Q-BN, which is amorphous in nature. The undercooling can be controlled by varying the thermal conductivities of as-deposited h-BN and substrate (sapphire) and laser energy density (0.6-1.0 Jcm^{-2}). Various state-of-the-art characterization techniques are used to determine the morphology, bonding characteristics, temperature and size-dependent phonon vibrational modes, and crystal structure (twinning and crystal orientation *w.r.t* the substrate) of c-BN. Unpolarized micro-Raman spectroscopy, SEM, TEM, EELS, and EBSD were performed on the nano and microstructures of c-BN. Horiba Xplora PLUS confocal Raman microscope (0.5 μm spatial resolution) in conjunction with Labspec software were used to perform the temperature and size-dependent Raman studies in nano and micro c-BN. The excitation source was a 532 nm laser of the Raman instrument was calibrated using a crystalline Si wafer (Raman-active peak at 520.6 cm^{-1}) prior to the measurements. The temperature-dependent Raman measurements were performed in the Linkam stage (variable temperature stage purged with Ar) attached to the Raman microscope. For accurate measurements, the stage was thermally

stabilized for 2 minutes prior to Raman spectra acquisition. FEI Verios 460L SEM (having sub-nanometer resolution) was used to characterize the laser irradiated films. FEI Quanta 3D FEG microscope having a dual beam technology, which uses both electron and ion beam guns was used for preparing thin cross-sectional samples for TEM and EELS. EBSD measurements were performed in the above-mentioned microscope using an EBSD HKL Nordlys detector. The lateral resolution of the EBSD detector was less than 10 nm, and it can map out the Kikuchi diffraction pattern (for determination of structures) of nano and microstructures of c-BN. JEOL-2000FX and 2010F STEM/TEM (point-to-point TEM resolution 0.18nm; STEM-Z resolution 0.08nm with information limit of 0.06nm) were used in conjunction with EELS, to collect high-resolution TEM images, bright field imaging, micro-diffraction (selected area electron diffraction), and EELS spectra with a resolution of 0.15 eV. This helped to determine the crystal structure (orientation and twinning) and bonding characteristics in c-BN, which is formed by our highly non-equilibrium technique.

3. Results and discussion

3.1. Formation of nano- and micro c-BN :

Figures 1(a-d) show the formation of nano, micro and large-area c-BN formation from h-BN by the PLA process. The average size of the nanocrystals is ~90 nm. The formation of c-BN nanocrystals is dependent on the nucleation and growth velocity, which are controlled by undercooling during the PLA. The PLD deposited h-BN is of nanocrystalline nature, which is melted in a highly undercooled state (at 2800 K) during the PLA process. This leads to a complete conversion of h-BN to c-BN after the quenching from melt. The growth velocity (v) is directly related to the undercooling by the equation: $v = \frac{D_{\propto} f}{\lambda f_D}\left(1 - e^{\frac{(T_m - T_u)\Delta S}{kT}}\right)$, where, $D_{\propto}, f, \lambda,$ f_D, k, T, T_m, T_u and ΔS denote the liquid diffusivity of the BN (~10^{-8} m^2/sec in liquid state),

fraction of the available sites, atomic jump distance, geometrical factor associated with diffusion, Boltzmann constant, temperature, melting temperature, undercooling temperature, and the change in entropy, respectively. An increase in the value of T_u decreases the value of chemical free energy barrier for h-BN to amorphous Q-BN or crystalline c-BN phase transformation. This also increases the velocity of the melt-front. Therefore, the values of undercooling dictate the formation of amorphous Q-BN and crystalline c-BN from the BN melt. If the cooling rate is slow (low undercooling and low solidification velocity), crystalline c-BN is formed whereas with high cooling rates (large undercooling and large solidification velocity), amorphous Q-BN is formed. For facilitating the homogeneous nucleation of c-BN from the super undercooled state, the Gibbs free energy of the c-BN nuclei (ΔG_T) is governed by the equation: $\Delta G_T = -\frac{4}{3}\pi r^3 \Delta G_v + 4\pi r^2 \gamma_s$, where ΔG_v denotes the difference between free energies per unit volume of c-BN solid and the super undercooled liquid, γ_s denotes c-BN/super undercooled liquid interfacial energy, and r denotes nuclei radius (of c-BN). Thermodynamically, the nucleation of c-BN is difficult due to large values of γ_s. But using ultrafast non-equilibrium techniques, undercooling can be achieved which assists the crystal nucleation. The critical size of nuclei (r^*) can also be calculated (at $\frac{d\Delta G_T}{dr} = 0$) using: $r^* = \frac{2\gamma_s T_m}{\Delta H_f \Delta T}$, where T_m, ΔH_f, and ΔT denote melting point, latent heat of fusion, and undercooling, respectively. Similarly, the critical free energy (ΔG_T^*) for the formation of r^* can also be calculated and is proportional to ΔT^{-2}. The driving force for the solidification is directly proportional to the degree of undercooling. With the increase in undercooling, there is a decrease in the value of ΔG_T^* and r^*. This facilitates an increase in the rate of nucleation (at large undercooling values). This leads to amorphization (large undercooling) and twinned (medium undercooling) and defect-free crystal (small undercooling) formation (figure 1(e)). The degree of undercooling can be controlled by laser parameters

(energy density 0.6-1.0 Jcm^{-2}) and thermal conductivities of the as-deposited thin film and the substrate. However, it should also be noted that, for heterogeneous nucleation of c-BN (on *c*-sapphire substrate), low undercooling favors crystal growth as the critical free energy for the formation of r^* is lower as compared to homogeneous nucleation. This facilitates the formation of c-BN crystals closer to T_m, where crystal growth is predominant than nucleation.[27] Figure 1(b) depicts the initial stages of formation of c-BN microcrystallites (shown by arrow) from nanocrystalline h-BN (inset of figure 1(b)) on *c*-sapphire. The size of the c-BN crystals is ~1 μm. When sufficient time for growth (from the BN melt) is given, large micro-crystals (~5 μm) and single-crystal films of c-BN are formed (figure 1(c) and (d)). The inset in figure 1(c) indicates the formation of micro c-BN from Q-BN,[25] which is amorphous in nature (formed at high undercooling conditions). The single-crystal films of c-BN can be grown directly on *c*-sapphire, when super undercooled state of BN grows directly on sapphire, which provides a template for the epitaxial growth by domain matching epitaxy paradigm.[26] The growth velocity (v_{growth}) in the liquid BN phase determines the dimension of the single crystal c-BN formed. The growth velocity is calculated to be ~10 msec^{-1} using: $v_{growth} = K_s T_m / ((D\tau)^{0.5} \rho L)$, where $K_s, T_m, D, \rho,$ and L denote thermal conductivity of sapphire substrate at 2800 K (5.65 Wm^{-1}K^{-1}), melting point of BN (2800 K), thermal diffusivity (10^{-8} m^2/sec), density of liquid c-BN (3.45 gcm^{-3}), latent heat of c-BN (1800 Jg^{-1}). In the highly superundercooled state, the rate of nucleation (r_n) is extremely high.[28] The rate of nucleation can be calculated using:

$r_n = C_1 \exp\left({-C_2} \big/ {(1 - T/T_m)^2 T/T_m} \right)$, where C_1 and C_2 are constants. Therefore, when $T \ll T_m$,

the rates of nucleation are extremely high. The formation of large microcrystals of c-BN occurs due to explosive crystallization. The process of explosive crystallization is exothermic in nature,

thereby leading to a stable growth of microcrystals (of c-BN). Figure 1(d) shows the formation of large-area c-BN with the inset showing large microcrystals (~5 μm) of c-BN, which are highly faceted. Therefore, direct conversion of h-BN to c-BN is possible using the highly non-equilibrium technique.

3.2. Transmission electron microscopy and electron backscatter diffraction:

High-resolution TEM (figure 2(a)) and SAED (figure 2(b)) studies of micro and nano c-BN show the presence of twins (crystal defects). The nano-twinned structures are energetically more favorable than their nanograin counterparts (as the energy of twin boundaries is an order of magnitude less than that of grain boundaries).[29] The presence of twin boundaries also enhances the hardness of a material (as twins are a barrier to dislocation glides). In the present work, we have demonstrated the formation of twins in nano and micro c-BN by controlling the extent of undercooling. With increasing the values of undercooling (by changing the thermal conductivities of as-deposited nanocrystalline h-BN and substrate and laser parameters) we have achieved a highly twinned structure. The bright field HRTEM image in figure 2(a) shows the presence of twins and high dislocation density in micro c-BN. The dislocations terminate in the twinned region (twin thickness < 100 nm). Since the {111} twins are visible the edge dislocations are of a/6<112> type. The top left inset and right bottom inset in figure 2(a) depict the formation of twins in nano c-BN (twin thickness < 5 nm). The top right inset in figure 2(a) illustrates the heterogeneous nucleation of epitaxial c-BN (formed by rapid crystallization) on sapphire. The SAED pattern of c-BN (figure 2(b)) depicts the <110> cross-section, which has characteristics diffraction spots from {111} and {002} planes. The <110> texture growth of c-BN is similar to that in Si formed under rapid unseeded crystallization.[30] The c-BN crystals are epitaxially aligned to the substrate (*c*-sapphire). The electron diffraction pattern of the substrate

(*c*-sapphire) is shown in the inset of figure 2(b). The SAED pattern depicts $< \bar{2}110 >$ cross-section of the substrate. The out-of-plane epitaxial arrangement is: <111> of c-BN aligned with <0001> sapphire. The in-plane epitaxial arrangements are: <110> c-BN // $< \bar{2}110 >$ sapphire and <112> c-BN // $< \bar{1}101 >$ sapphire. According to the DME paradigm,[31] to accommodate the planar lattice misfit, 16 ($\bar{2}110$) planes of sapphire match with 15 {110} half-planes of c-BN. The SAED pattern (figure 2(b)) also shows the presence of twin spots (marked in circles). The twin axis [$1\bar{1}1$] forms the twin spots $1/3(\bar{1}15)$, $1/3(1\bar{1}2)$, $2/3(1\bar{1}4)$, $1/3(7\bar{7}1)$ of ($1\bar{1}\bar{1}$), (002), ($2\bar{2}0$), and ($1\bar{1}3$) diffraction spots, respectively (shown in figure 2(b)). Similar twinned structures in Si were also observed in previous studies.[32] There occurs a rotation of 180^0 about the twin axis to form the twin spots. For cubic materials, the reciprocal lattice vectors of twin spots are calculated using the equation (1):

$$h^* = \frac{p(ph+2qk+2rl)-h(q^2+r^2)}{p^2+q^2+r^2} \tag{1}$$

where, [pqr] is the twin axis and hkl is rotated 180^0 about the twin axis. The twin density for micro and nano c-BN is calculated to be $\sim 10^8$ and 10^{12} cm^{-2}, respectively. The SEM images in figures 2(c)-(f) indicate twinning in c-BN formed by ultrafast quenching and solidification technique. The SEM images show high density of twinning in c-BN. The mirroring of crystal facets is indicative of the twinned structure. These heavily twinned structures result from super undercooling process, where the solidification velocities are less than that in Q-BN but more than single-crystal c-BN formations. The size of c-BN crystallites is $\sim 0.5 \times 5 \times 5$ μm^3. Since the melt lifetime is ~150 ns, the growth velocities exceed 3 msec^{-1}. This indicates rather rapid recrystallization of c-BN from the superundercooled state. Such high values of crystal growth rate also indicate laser-induced liquid phase growth of c-BN from h-BN. Figure 3 depicts the

electron backscatter (Kikuchi) diffraction performed using EBSD detector in FEI microscope. This technique provides electron diffraction pattern to determine the phase, crystallinity, and orientation of the phase formed (nano or micro) with respect to the substrate. The resolution of this technique (~10 nm) is directly proportional to the probe size of the incident electron beam, which can be controlled by accelerating voltage and beam current. The secondary electron images and Kikuchi diffractions of nano c-BN from two different spots are shown in figures 3(a-d). A similar analysis is performed on micro c-BN and is shown in figure 3(e). The simulated Kikuchi patterns (of c-BN) are overlaid on the diffraction patterns for a better representation of the diffracting planes. As it is evident from figure 3, the Kikuchi bands are more prominent in the case of micro c-BN due to an increase in the electron interaction volume of electrons with the sample (in micro c-BN). The dynamical simulations of the EBSD Kikuchi pattern for regions A and B are shown in figure 3 (f-g). The crystal orientations (shown in the inset of figure 3(f-g)) correspond to twin formation in the c-BN structure. When the solidification rates exceed certain values (>5 msec^{-1}), twinned structures of c-BN are formed. Similar twin formations are also experimentally shown for Si, where the maximum melt growth is observed for (001) as compared to (111) close-packed surfaces.[32-34] The production of these defects can also enhance the crystal growth rate, particularly for slower growing surfaces (by nucleation). The formation of twins predominantly occurs prior to complete amorphization.[33] Therefore, the defect density in nano c-BN (formed at higher undercooling) should be considerably larger than that in micro c-BN (formed near T_m), which is discussed in detail below. If the solidification rates are increased to higher values (>10 msec^{-1}), the transient melt is highly super undercooled and rapid growth defect multiplication takes place at the melt/solid interface. This leads to the formation of highly

dense amorphous Q-BN thin films, which have been shown to possess novel mechanical and electrical properties.

3.3. Electron energy-loss spectroscopy and Raman spectroscopy:

The details of bonding characteristics (of c-BN) are probed using electron energy-loss spectroscopy (figure 4(a)). The background corrected spectrum along with the experimental spectrum and background are shown in figure 4(a). The c-BN formed *via* highly non-equilibrium synthesis technique shows the B-K edge peaks at 198.2 (σ* antibonding state), 216.6, and 234.5 eV. The EEL spectrum also shows N-K edge peaks at 408.4 (σ*) and 436.7 eV. The characteristic fine post-edge structures in EELS indicate long-range periodicity (crystalline structure) in c-BN. The long-range periodic structure of crystalline c-BN gives rise to modulation to the density-of-states, as it is evident from the σ* region in EELS. The high optical band gap of c-BN (6.4 eV) gives rise to the core-hole effect, which is also observed from the EELS profile of c-BN.[35] In high band gap materials, the core-hole effect is dominant, as the rescreening of the hole by valence electrons is nor complete. Other prominent phases of BN, h-BN and w-BN have their characteristic B and N K-edges at 192 and 402 eV ($1s$ to π* transition) which are completely absent in the EEL spectra of laser annealed c-BN. This also proves a complete conversion of h-BN to c-BN *via* laser melting and ultrafast quenching process. The temperature-dependent vibrational modes (of the synthesized nano and micro c-BN) are studied using Raman spectroscopy. Figure 4(b) indicates the unpolarized Raman spectra of micro and nano c-BN synthesized *via* the highly non-equilibrium technique. The Raman spectrum of micro c-BN indicates phonon vibrational modes centered at 1055 (transverse optical: TO) and 1305 (longitudinal optical: LO) cm^{-1} (in figure 4(b) and 5(a), respectively). Interestingly, in nano c-BN (as compared to micro c-BN) there occurs ~35 cm^{-1} red-shift of the TO mode due to phonon

confinement and $\sim$20 cm^{-1} blue-shift of the LO mode due to electro-optical effect, which is discussed in detail below. The Raman peak $\sim$1325 cm^{-1} in nano c-BN spectrum is not due to the presence of BC$_2$N phases (which also have peak $\sim$1325 cm^{-1}).[36] Furthermore, BC$_2$N phase has no Raman-active peak $\sim$1020 cm^{-1}. BC$_2$N phases also have distinct electron diffraction pattern and EELS, which are not observed in the present study. The blue-shift of LO mode in nano c-BN can be due to internal strain fluctuations [37] and formation of twinned structure. It is well known that the size and shape of nanoparticles affect the Raman spectra.[38] If the size of the nanoparticles is less than the wavelength of the laser (532 nm), the induced electromagnetic field in the nanoparticle strongly influences the Raman scattering modes. The electromagnetic field can influence the electro-optical effect in c-BN nanoparticles, thereby causing the blue-shift. The Raman spectra of nano and micro c-BN show no evidence of peak $\sim$1365 cm^{-1} (E$_{2g}$ mode), which is characteristics of h-BN. The spectra also indicate a complete absence of peaks $\sim$1260 cm^{-1}, which is predominantly observed for amorphous BN entities. These results are consistent with a complete conversion of h-BN to c-BN *via* melting and super undercooling process. Since c-BN has a zinc blende structure, it has one optical phonon mode at Γ which is Raman-active. Due to the ionic character of BN, this triply degenerate vibrational mode splits into TO and longitudinal LO modes. In the case of h-BN, there is no splitting of the Raman-active mode centered at 1365 cm^{-1}, due to the planar structure of h-BN (where the contributions from the two planes cancel out each other). Unlike TO phonons, the intensity of LO phonons can be enhanced by external electrical field. The LO modes are strongly affected by light due to the electro-optical (EO) effect.[39] The TO modes are only affected by the deformation-potential interaction, and thereby provides an excellent marker for size, temperature, and pressure dependent studies.[40] The electro-optical effect is predominantly observed in nanomaterials, where symmetry-breaking

occurs due to reduction in size (phonon-confinement). The study of electro-optical effect in semiconductors is interesting as it leads to the development of novel optoelectronic materials (optical modulators and waveguides).[41] The EO effect is determined by the Faust-Henry coefficient (C), which is calculated using the equation (2):

$$C = -\left[\left|2\frac{I_{LO}}{I_{TO}}\cdot\frac{\omega_{LO}}{\omega_{TO}}\cdot\left(\frac{\omega_l-\omega_{TO}}{\omega_l-\omega_{LO}}\right)^3\right| - 1\right]^{-1}\left[\frac{\omega_{LO}^2-\omega_{TO}^2}{\omega_{TO}^2}\right] \tag{2}$$

where, I_{LO}, ω_{LO}, and ω_l indicate intensity, phonon frequency, and incident laser frequency, respectively. The ratio of ionic and electronic term contributing to the EO effect is directly proportional to C. The value of C (at 300 K) is calculated as -0.83 and 4.16 for micro and nano-cBN as compared to -1.53 for mm-sized c-BN [40] prepared by HPHT techniques. This shows a higher ionic character in nano c-BN as compared to micro c-BN. Therefore, the splitting of triply degenerate vibrational modes (TO and LO) at the Brillouin zone is increased in nano c-BN. There occurs a drastic change in the value of C to -0.21 (in nano c-BN) at 78 K. This requires a further study of the phonon scattering process in nano c-BN, which is discussed below.

3.4. Temperature- and size-dependent Raman measurements:

Measurements of temperature-dependent Raman shifts and change in line widths help in determining the type of phonon-interactions in materials. Previous results in c-BN have confirmed interesting Raman shifts and change in line widths at higher temperatures (above 500 K),[42,43,44,45] but no studies at cryogenic temperatures. However, low-temperature applications of c-BN based electronic devices require a detailed study of the material properties (phonon-interaction) for a better understanding. As it is evident from figures 4(c) and (d), there is a considerable shift of Raman peak (TO mode) to higher wavenumbers (blue-shift) with a decrease in temperature (300 to 78 K) in nano c-BN as compared to micro c-BN. Similar behavior of blue-

shift is also found for the LO mode (figures 5(b) and (c)). There is also a decrease in the Raman linewidths with decrease in temperature in c-BN. The decrease in linewidths is more prominent in micro c-BN as compared to nano c-BN. The temperature-dependent Raman shifts and change in linewidths can be understood in terms of an oscillator (the molecule) that interacts with the anharmonic potential (created by the electric field) within which the atoms move. At lower temperatures, there is a decreased phonon-phonon interaction, thereby resulting in less scattering and higher lifetime of these optical phonons. This leads to a decrease in the Raman line width with decreasing temperature. This phenomenon is well-established in micro c-BN which has well-defined phonon interactions. Therefore, the decrease in linewidth with decreasing temperature is prominently observed in micro crystals of c-BN. The temperature-dependent Raman shift and change in linewidths in nano c-BN are discussed in detail below.

The change in Raman frequency with crystallite size is investigated (figure 6) using the theory of phonon confinement as described in the spatial correlation model.[46,47] According to this model, for the case of ideal crystals, only phonons near the center of the Brillouin zone ($q = 0$) contribute to the Raman spectrum. In a real crystal, phonons can be confined by grain boundaries, stacking faults, impurities, *etc*. This results in the uncertainty of phonon momentum and therefore phonons having $q \neq 0$ contribute to the Raman spectrum. As discussed above, since the TO mode is affected only by the deformation-potential interaction, Raman peak fitting is performed in this mode. The normalized intensity ($I(\omega)$) of a Raman-active peak can be fitted using the equation (3):

$$I(\omega) \approx \int_0^1 \frac{\exp(-(qS/4\pi)^2)4\pi q^2\,dq}{[\omega - \omega(q)]^2 + [\Gamma_0/2]^2} \tag{3}$$

where, $\omega(q)$, S, and Γ_0 indicate one-dimensional phonon dispersion curve, correlation length

(defect-free phonon propagation length or mean free path), and natural linewidth (2.1 cm^{-1}) of

micro-sized strain free c-BN, respectively. For c-BN crystals having twins or other crystal

defects, the mean free path of phonon (S) will be less than the size of the crystal. The phonon

dispersion curve for the TO mode can be calculated using the equation (4):

$$\omega(q) = \sum_{n=0}^{n=6} A + B_n \cdot \left(\frac{q}{a} \cdot \pi\right)^n \tag{4}$$

where, a denotes the lattice constant of c-BN and A, B_n are the dispersion constants. The inset of

figure 6(a) shows the plot of phonon dispersion curve ($\omega(q)$) *vs* reduced wavevector (q/q_{max})

of TO mode in c-BN, calculated theoretically.[48] The value of q_{max} is $2\pi/a$. Therefore, at the

center of the Brillouin zone (Γ), $q = 0$ and at the face-center (X) of the crystal, $q = q_{max}$. As

discussed before, there is no Raman shift at $q = 0$ (Brillouin zone). There is a gradual decrease

in the value of Raman shift when q approaches q_{max}. The theoretical calculations provide a

better estimate of the curvature of $\omega(q)$, whereas the experimental approach gives an accurate

value of Raman shift at the Brillouin zone ($q = 0$). Therefore, the dispersion curve is rigidly

shifted to 1055 cm^{-1} at $q = 0$ from the theoretical calculations. As it is evident from the phonon

dispersion curve that a downshift of Raman frequency of the TO mode in c-BN is caused by the

deviation (or shift) from $q = 0$ point. A 35 cm^{-1} red-shift in nano c-BN corresponds to

$q/q_{max} = 0.37$, which contributes to the phonon vibrational modes in nano c-BN. On the other

hand, $q/q_{max} = 0.05$ contributes to the phonon vibrational modes in micro c-BN. Figure 6(a)

shows the fitted curves (equation (3)) along with the experimentally acquired (normalized)

Raman spectra of nano and micro c-BN. The curve fitting helps us to determine the correlation

lengths (S) in nano and micro c-BN. The correlation length is calculated as 50 and 24 nm for the

case of micro and nano c-BN, respectively. These values are in good agreement with the earlier calculated S values in micro and nano c-BN.[49] We have also plotted the intensity *vs* Raman shift for c-BN microcrystals having $S = 1000\ nm\ (or\ 1\ \mu m)$. As it is evident from figure 6(a), there is an increase in FWHM with decrease in S. This indicates that low values of S correspond to high values of defect density in a crystal. The plots of weighing function $(\exp(-(qS/4\pi)^2))$ *vs* correlation length (figure 6(b)) show an increasing influence of regions with large q for small correlation length to the shape of Raman peak. The temperature-dependent Raman shift (frequency) can be fitted using the polynomial equation: $v(T) = a_0 + a_1T + a_2T^2$, where a_0, a_1, and a_2 indicate coefficients. The fittings for LO and TO vibrational modes in nano c-BN are shown in figure 6(c). For the TO vibrational mode, the values of a_0, a_1, and a_2 are 1341.89 cm^{-1}, -0.08 cm^{-1}/K, and 1.19×10^{-4} cm^{-1}/K^2, respectively. For the LO vibrational mode, the values of a_0, a_1, and a_2 are 1025.93 cm^{-1}, -0.06 cm^{-1}/K, and 8.81×10^{-5} cm^{-1}/K^2, respectively. The values of the temperature-dependent coefficients for micro c-BN are $a_1 = -0.01$ and -0.003 cm^{-1}/K for TO and LO modes, respectively and $a_2 = -1.45 \times 10^{-5}$ and -1.46×10^{-5} cm^{-1}/K^2 for TO and LO modes, respectively.[45] The different values of temperature-dependent coefficients in nano and micro c-BN suggest different modes of phonon relaxation (in nano and micro c-BN), which is also related to the correlation length.

The temperature-dependent Raman shift is the result of both vibrational frequency change (as volume increases at higher temperature) and self-energy shift that arises from phonon coupling. The latter term can be defined as the change in the average vibrational energy at constant volume. The Raman shift due to thermal expansion ($v_G(T)$) can be calculated using the equation (5):

$$\nu_G(T) = \nu(0). exp\left(-M \int_0^T \alpha \, dT\right) \qquad (5)$$

where, $\nu(0)$ and α indicate Raman shift at 0 K and linear thermal expansion coefficient, respectively. The term M depends on the nature of vibrational mode and is equal to 4.5 for TO mode and 3.6 for LO mode.[50] The Raman shift due to thermal expansion is shown for the TO and LO modes in figure 7(a) and (b), respectively. As it is evident from the figures that there is an increase in the difference between the experimentally observed Raman shift and that due to volume expansion with an increase in temperature (up to 300 K). This is due to the self-energy (anharmonic contribution ($\nu_{an}(T)$)) of the system, which can be calculated using: $\nu_{an}(T) = \nu_{obs}(T) - \nu_G(T)$. In other strongly-bonded materials like diamond, $\nu_{an}(T)$ also behaves in a similar fashion. As it is evident from the inset of figure 7(b), the $\nu_{an}(T)$ contribution for LO mode is greater than that in TO mode. Earlier results have shown that in the case of micro c-BN, the $\nu_{an}(T)$ is more prominent in TO mode as compared to LO mode.[45] This may be because the optical-electric effect is pronounced in nano c-BN as compared to micro c-BN. The temperature-dependent Raman linewidth of the TO and LO modes in c-BN can be explained by an increased probability of phonon decay (at high temperatures). This occurs due to the increase in the phonon occupation at high temperatures. The TO mode can decay *via* three or three and four phonon processes. The temperature-dependent linewidth ($\Gamma(T)$) for a three and four phonon processes can be calculated using equation (6):

$$\Gamma(T) = A\left(1 + 2\left\{\exp\left(\frac{\square c\nu}{2kT}\right) - 1\right\}^{-1}\right) + B\left(1 + 3\left\{\exp\left(\frac{\square c\nu}{3kT}\right) - 1\right\}^{-1} + 3\left\{\exp\left(\frac{\square c\nu}{3kT}\right) - 1\right\}^{-2}\right)$$

(6)

where, A and B are constants and ν Raman frequency of the TO (or LO) mode at 300 K. For a

pure three-phonon process, $B=0$. As it is evident from the equation (6), that with decreasing

temperature, the Raman linewidth decreases and approaches the value of A for a three-phonon

process and (A+B) for three and four phonon processes (at T=0 K). Figures 7(c) and (d) indicate

that there occurs three- and four-phonon processes at low-temperatures (77-300 K) for TO and

LO modes in nano c-BN. Therefore, it is conclusively shown that the anharmonic effects in nano

c-BN cause Raman blue-shift, and the decrease in Raman linewidth with decreasing temperature

is caused by three- and four-phonon decay processes.

4. Conclusions:

In conclusion, we have successfully shown that nanocrystalline h-BN (~25 nm) can be converted

directly into phase-pure c-BN at ambient temperature and atmospheric pressure in air. The sizes

of c-BN (90 nm to 25 μm) and crystal twinning can be varied by changing the quenching rates,

which changes the nucleation and growth of c-BN. The selected area electron diffraction patterns

also indicate the formation of heavily twinned c-BN with $[1\bar{1}1]$ as the twin axis. The formation

of crystal twins predominantly occurs before the formation of amorphous Q-BN. The twin

density in nano c-BN (formed at higher undercooling) is calculated to be $\sim10^{12}$ cm^{-2}, which is

four-order larger than that in micro c-BN (formed near melting temperature). The temperature-

dependent Raman studies (300 to 78 K) show a considerable blue-shift of ~6 cm^{-1} in nano c-BN

as compared to micro c-BN. The spatial correlation model is also used to demonstrate the size-

effect of c-BN crystals on the Raman-active vibrational modes (TO and LO). The model is also

employed to calculate the correlation lengths (50 and 24 nm for the case of micro and nano c-

BN, respectively), which lead to a better understanding of the rapid-crystallization process from

the BN melt. The anharmonic effects in Raman frequency and decrease in Raman linewidths in

c-BN with decreasing temperature can also be caused by three and four phonon decay process. The atomic structure, bonding characteristics (σ^* antibonding electronic state), and phonon vibrational modes of the synthesized c-BN crystals have been studied by high-resolution SEM, TEM, EELS, EBSD, and temperature-dependent Raman spectroscopy. The twinned diamond with twinned c-BN structures will lead to potential ultrahard materials. We are collaborating with Prof. E. Riedo, CUNY, New York for the Modulated NanoIndentation (MoNI) method. This method has been used to measure the effective stiffness (indentation modulus) of Q-carbon structures (*harder* than diamond) while using CVD diamond and sapphire as standards.[51] The detailed mechanical properties of the c-BN structures will be reported elsewhere. We envision, that the controlled synthesis of nano and microstructures of twinned c-BN using nanosecond excimer laser and their temperature-dependent studies will have a significant impact on low-temperature electrical and mechanical devices.

Acknowledgments:

Conflict of Interest

The authors declare no competing financial interest.

References:

1   C. B. Samantaray and R. N. Singh, *Int. Mater. Rev.*, 2005, **50**, 313–344.

2   Y. Tian, B. Xu, D. Yu, Y. Ma, Y. Wang, Y. Jiang, W. Hu, C. Tang, Y. Gao, K. Luo, Z. Zhao, L.-M. Wang, B. Wen, J. He and Z. Liu, *Nature*, 2013, **493**, 385–388.

3   X. W. Zhang, H.-G. Boyen, N. Deyneka, P. Ziemann, F. Banhart and M. Schreck, *Nat. Mater.*,

2003, **2**, 312–315.

4   J. Zhao and P. Shrotriya, *Procedia Manuf.*, 2016, **5**, 747–760.

5   X. W. Zhang, *Thin Solid Films*, 2013, **544**, 2–12.

6   J. Yu, Z. Zheng, H. C. Ong, K. Y. Wong, S. Matsumoto and W. M. Lau, *J. Phys. Chem. B*, 2006, **110**, 21073–21076.

7   S. N. Monteiro, A. L. D. Skury, M. G. de Azevedo and G. S. Bobrovnitchii, *J. Mater. Res. Technol.*, 2013, **2**, 68–74.

8   O. A. Shenderova and D. M. Gruen, *Ultrananocrystalline diamond : synthesis, properties and applications*, William Andrew, 2012.

9   X. W. Zhang, H.-G. Boyen, N. Deyneka, P. Ziemann, F. Banhart and M. Schreck, *Nat. Mater.*, 2003, **2**, 312–315.

10   M. Okamoto, Y. Utsumi and Y. Osaka, *Jpn. J. Appl. Phys.*, 1990, **29**, L1004–L1006.

11   K. Hirama, Y. Taniyasu, S. Karimoto, Y. Krockenberger and H. Yamamoto, *Appl. Phys. Lett.*, 2014, **104**, 92113.

12   L. Rao and R. B. Kaner, *Inorg. Chem.*, 1994, **33**, 3210–3211.

13   T. Endo, O. Fukunga and M. Iwata, *J. Mater. Sci.*, 1981, **16**, 2227–2232.

14   D. R. McKenzie, W. D. McFall, W. G. Sainty, C. A. Davis and R. E. Collins, *Diam. Relat. Mater.*, 1993, **2**, 970–976.

15   X. W. Zhang, H.-G. Boyen, P. Ziemann, M. Ozawa, F. Banhart and M. Schreck, *Diam. Relat. Mater.*, 2004, **13**, 1144–1148.

16   Y. Tian, B. Xu, D. Yu, Y. Ma, Y. Wang, Y. Jiang, W. Hu, C. Tang, Y. Gao, K. Luo, Z. Zhao, L.-M. Wang, B. Wen, J. He and Z. Liu, *Nature*, 2013, **493**, 385–388.

17   J. L. Liu and B. Sājid, *Advanced nanomaterials and their applications in renewable energy*, .

18   R. B. Mathur, *Carbon nanomaterials : synthesis, structure, properties and applications*, CRC Press, 2017.

19   V. V. Zhirnov, O. A. Shenderova, D. L. Jaeger, T. Tyler, D. A. Areshkin, D. W. Brenner and J. J.

Hren, *Phys. Solid State*, 2004, **46**, 657–661.

20 J. Narayan, A. Bhaumik, S. Gupta, A. Haque and R. Sachan, *Mater. Res. Lett.*, 2018, **6**, 353–364.

21 X. Liu, X. Chen, H.-A. Ma, X. Jia, J. Wu, T. Yu, Y. Wang, J. Guo, S. Petitgirard, C. R. Bina and S. D. Jacobsen, *Sci. Rep.*, 2016, **6**, 30518.

22 V. Z. Turkevich, *J. Phys. Condens. Matter*, 2002, **14**, 10963–10968.

23 J. Narayan and A. Bhaumik, *J. Appl. Phys.*, 2015, **118**, 215303.

24 J. Narayan and A. Bhaumik, *APL Mater.*, 2015, **3**, 100702.

25 J. Narayan and A. Bhaumik, *APL Mater.*, 2016, **4**, 20701.

26 J. Narayan and B. C. Larson, *J. Appl. Phys.*, 2003, **93**, 278.

27 D. A. Porter and K. E. Easterling, *Phase transformations in metals and alloys*, Chapman & Hall, 1992.

28 J. Narayan and C. W. White, *Appl. Phys. Lett.*, 1984, **44**, 35.

29 X. Huang, N. Hansen, N. Tsuji and K. Lu, *Science (80-.).*, 2006, **312**, 249–251.

30 J. Narayan, *J. Appl. Phys.*, 1982, **53**, 8607–8614.

31 J. Narayan and B. C. Larson, *J. Appl. Phys.*, 2003, **93**, 278.

32 A. G. Cullis, N. G. Chew, H. C. Webber and D. J. Smith, *J. Cryst. Growth*, 1984, **68**, 624–638.

33 A. G. Cullis, H. C. Webber and N. G. Chew, *Appl. Phys. Lett.*, 1983, **42**, 875–877.

34 A. G. Cullis, H. C. Webber and N. G. Chew, *Appl. Phys. Lett.*, 1982, **40**, 998–1000.

35 D. N. Jayawardane, C. J. Pickard, L. M. Brown and M. C. Payne, *Phys. Rev. B*, 2001, **64**, 115107.

36 X.-F. Zhou, J. Sun, Q.-R. Qian, X. Guo, Z. Liu, Y. Tian and H.-T. Wang, *J. Appl. Phys.*, 2009, **105**, 93521.

37 R. Cuscó, J. Ibáñez, E. Alarcón-Lladó, L. Artús, T. Yamaguchi and Y. Nanishi, *Phys. Rev. B*, 2009, **79**, 155210.

38 E. O. Schäfer-Nolte, T. Stoica, T. Gotschke, F. A. Limbach, E. Sutter, P. Sutter, D. Grützmacher and R. Calarco, *Nanotechnology*, 2010, **21**, 315702.

39 W. D. Johnston and I. P. Kaminow, *Phys. Rev.*, 1969, **188**, 1209–1211.

40   S. Reich, A. C. Ferrari, R. Arenal, A. Loiseau, I. Bello and J. Robertson, *Phys. Rev. B*, 2005, **71**, 205201.

41   L. Prussel and V. Véniard, *Phys. Rev. B*, 2018, **97**, 205201.

42   A. F. Goncharov and J. C. Crowhurst, *J. Low Temp. Phys.*, 2005, **139**, 727–737.

43   A. F. Goncharov, J. C. Crowhurst, J. K. Dewhurst and S. Sharma, *Phys. Rev. B*, 2005, **72**, 100104.

44   T. Kawamoto, K. N. Matsukage, T. Nagai, K. Nishimura, T. Mataki, S. Ochiai and T. Taniguchi, *Rev. Sci. Instrum.*, 2004, **75**, 2451–2454.

45   Herchen and Cappelli, *Phys. Rev. B. Condens. Matter*, 1993, **47**, 14193–14199.

46   P. Parayanthal and F. H. Pollak, *Phys. Rev. Lett.*, 1984, **52**, 1822–1825.

47   S. K. Gupta and P. K. Jha, *Solid State Commun.*, 2009, **149**, 1989–1992.

48   K. Karch, F. Bechstedt, P. Pavone and D. Strauch, *Phys. B Condens. Matter*, 1996, **219**–**220**, 445–447.

49   T. Werninghaus, J. Hahn, F. Richter and D. R. T. Zahn, *Appl. Phys. Lett.*, 1998, **70**, 958.

50   J. A. Sanjurjo, E. López-Cruz, P. Vogl and M. Cardona, *Phys. Rev. B*, 1983, **28**, 4579–4584.

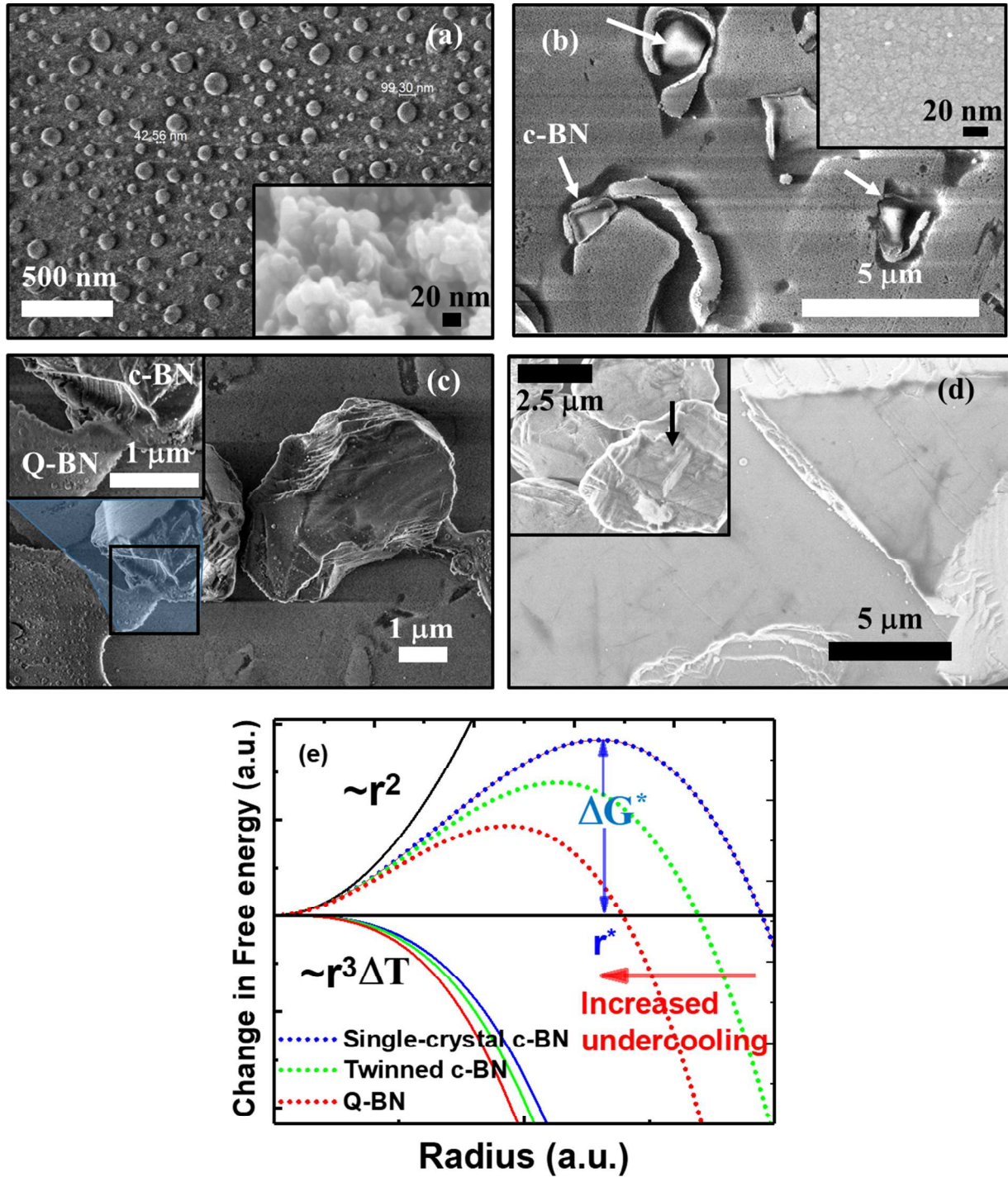51   J. Narayan, S. Gupta, A. Bhaumik, R. Sachan, F. Cellini and E. Riedo, *MRS Commun.*, 2018, 1–9.

Figure 1: FESEM of (a) nano c-BN formed after pulsed laser annealing (PLA) with the inset showing dense nanostructures of c-BN, (b) Initial stages of formation of micro c-BN with the inset showing nanocrystalline (~25 nm) h-BN, which is converted to phase-pure c-BN, (c) Formation of large micro-crystals of phase pure c-BN with the inset showing the transformation of Q-BN to c-BN, (d) Large-area c-BN formed after the PLA process with the inset showing highly faceted crystal structure of c-BN, and (e) Change in Gibbs free energy *vs* radius showing the formation of twinned c-BN by increasing the degree of undercooling.
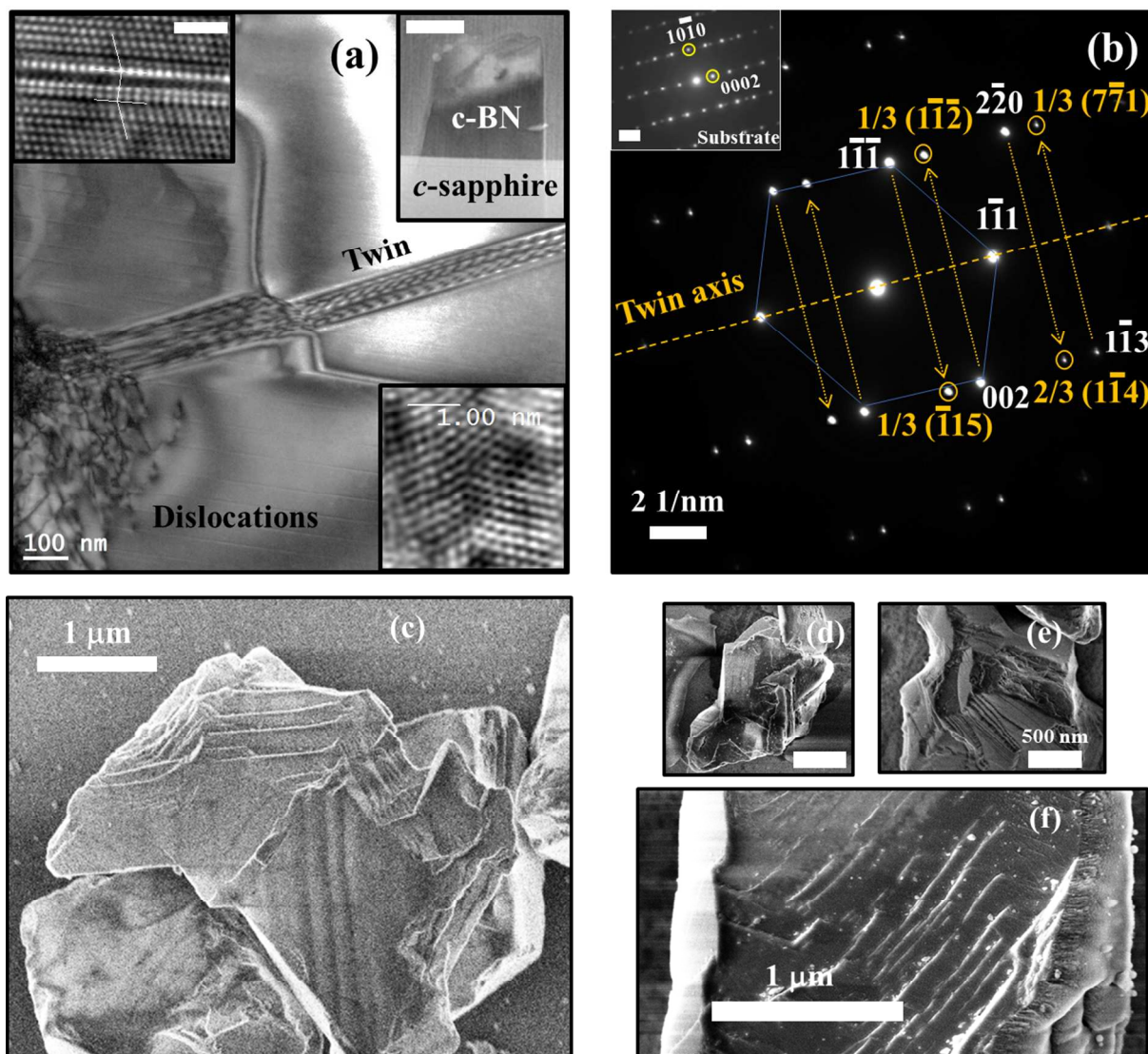
Figure 2: (a) HRTEM of c-BN showing twins and dislocation with the top left inset showing twin in micro c-BN, top right inset showing epitaxial growth of c-BN on c-sapphire, and lower inset showing twin in nano c-BN, (b) Selected area electron diffraction (SAED) pattern of twinned c-BN showing the twin axis and twin diffraction spots (with the inset showing <-2110> diffraction of the *c*-sapphire substrate), (c)-(f) FESEM of twins in various structures of c-BN formed after PLA. By changing the undercooling, twinning of c-BN is formed. The scale bars in top left inset and top right inset of figure (a) are 1 and 100 nm, respectively.
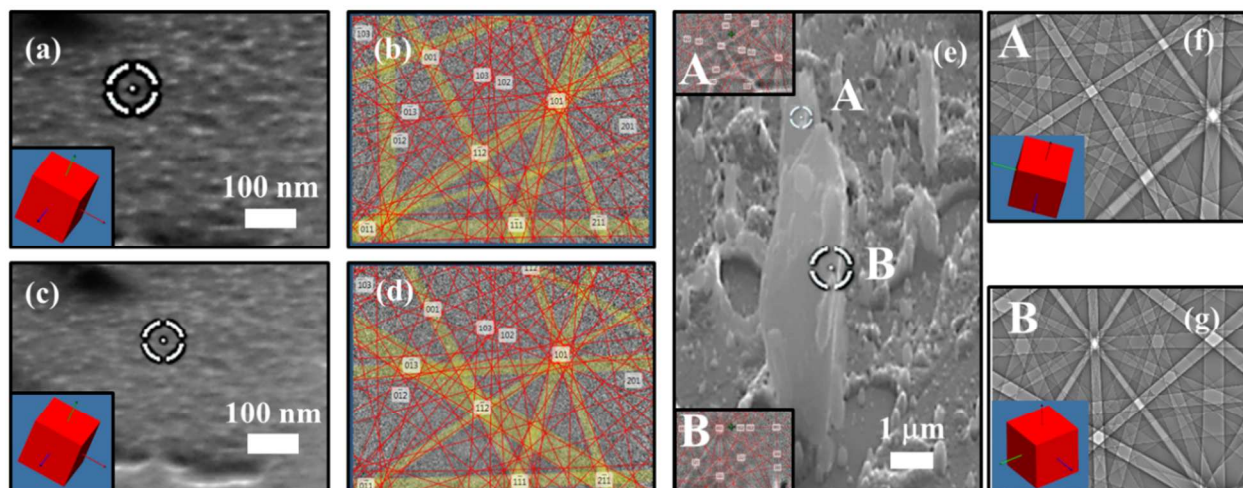
Figure 3: (a) and (c) Secondary electron images of nano c-BN, (b) and (d) EBSD Kikuchi pattern of nano c-BN showing the characteristic Kikuchi pattern of c-BN in red, (e) Secondary electron image of micro c-BN with the insets showing Kikuchi patterns of micro c-BN from region A and B, and (f-g) Dynamical simulation of the EBSD Kikuchi patterns for regions A and B with the inset showing crystal orientation.
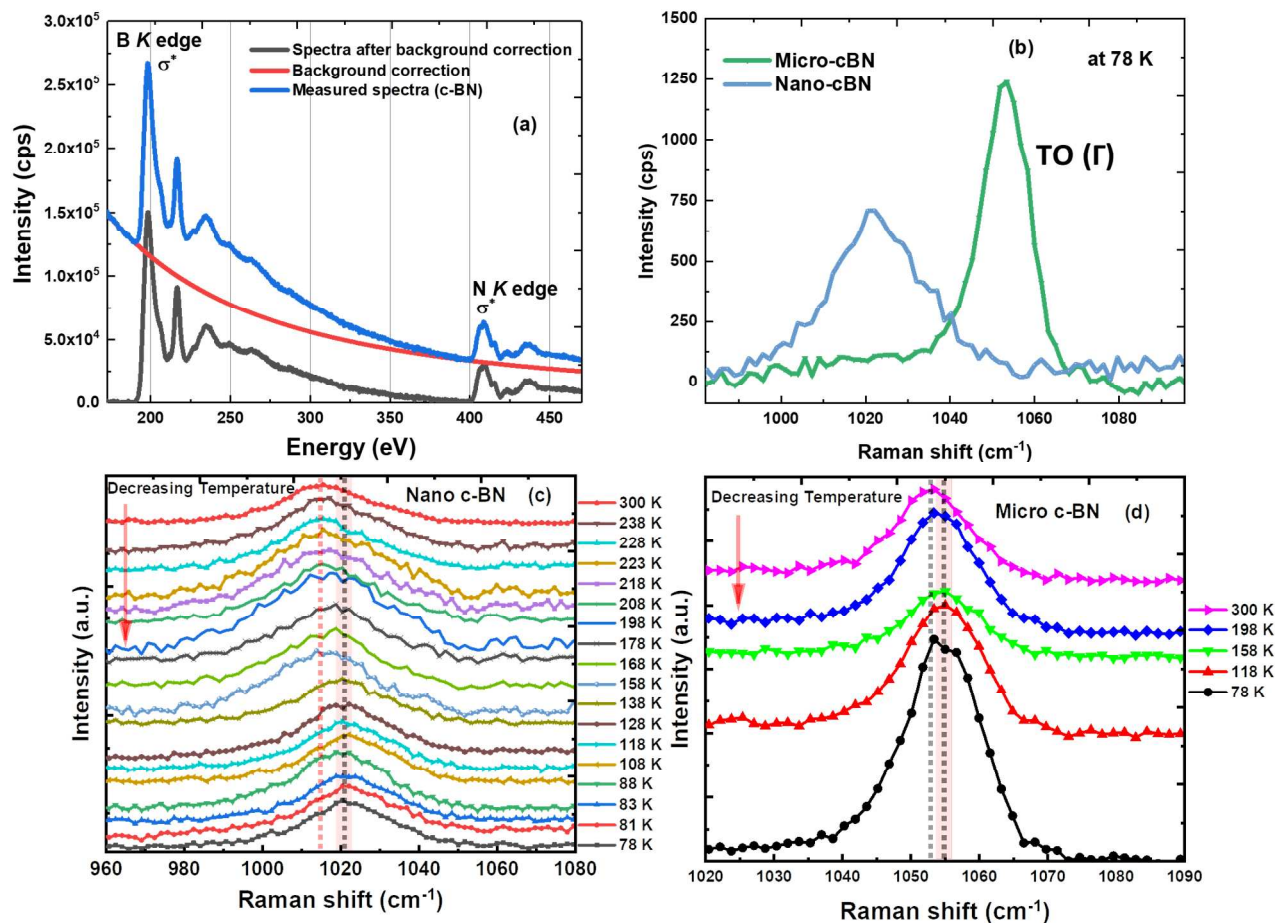
Figure 4: (a) Core-loss EELS of phase pure c-BN showing antibonding electronic states (σ*) of B and N, (b) Raman spectra of nano and micro c-BN at 78 K showing TO (Γ) vibrational mode, (c) Temperature-dependent Raman shift in nano c-BN, and (d) Temperature-dependent Raman shift in micro c-BN. As it is clearly evident that there is a considerable blue-shift in nano c-BN with decreasing temperature as compared to micro c-BN. The width of the red window is same in figures (c) and (d).
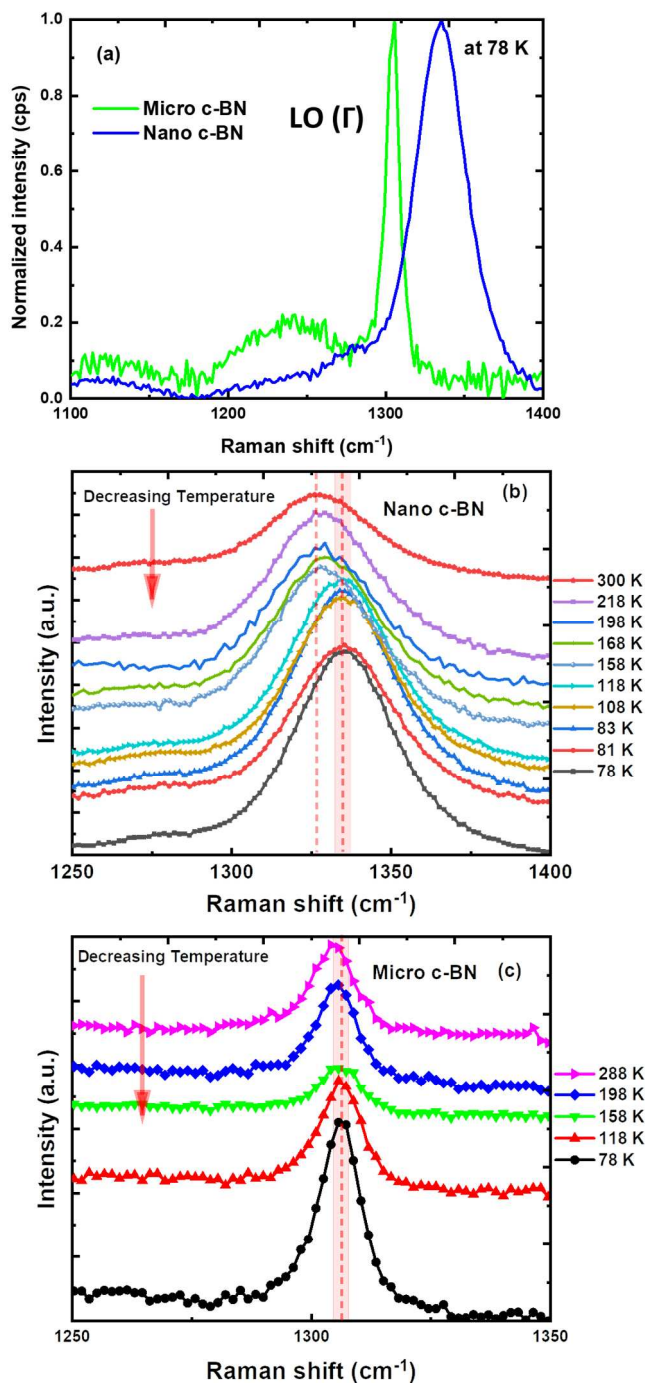
Figure 5: (a) Normalized Raman spectra of nano and micro c-BN at 78 K showing LO (Γ) vibrational mode, (b) Temperature-dependent Raman shift in nano c-BN, and (c) Temperature-dependent Raman shift in micro c-BN. As it is clearly evident that there is a considerable blue-shift in nano c-BN with decreasing temperature as compared to micro c-BN. The width of the red window is same in figures (b) and (c).
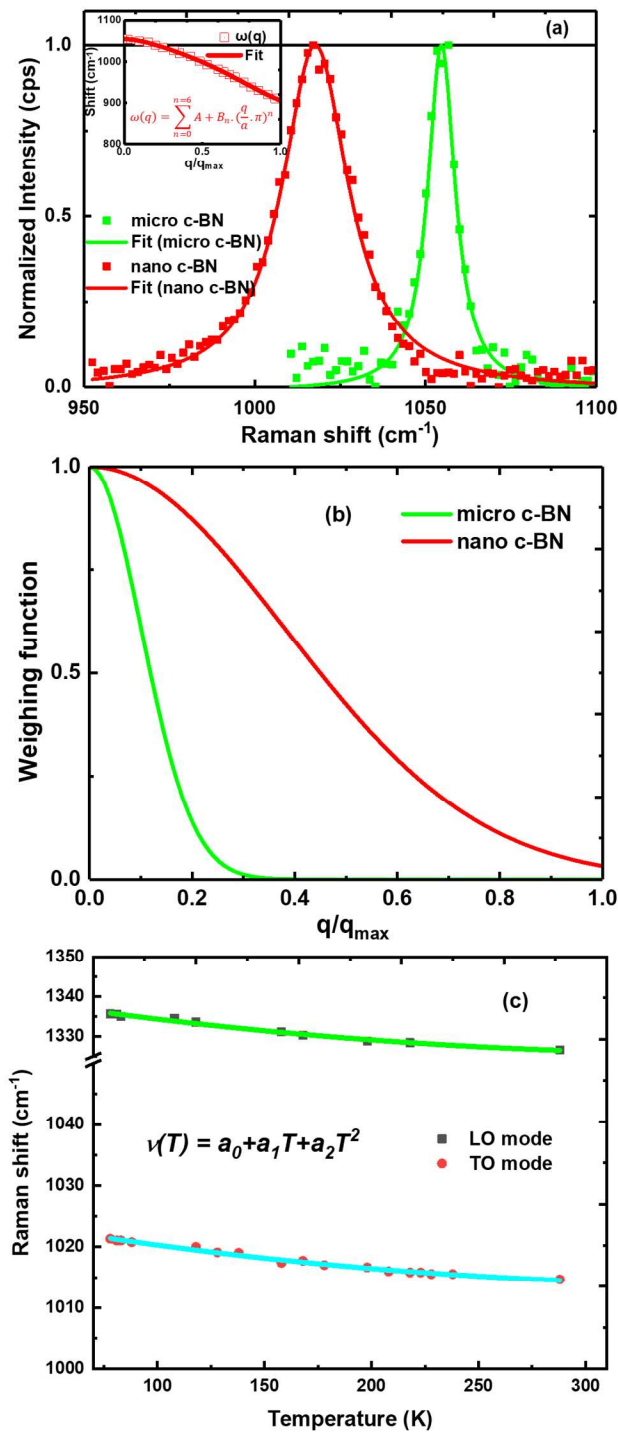
Figure 6: (a) Modeling of normalized intensity *vs* Raman shift (using spatial correlation model) in nano and micro c-BN formed after PLA with the inset showing theoretically calculated phonon dispersion (Raman shift *vs* q/q_{max}) for TO mode in c-BN, (b) Weighing function *vs* q/q_{max} for nano and micro c-BN, and (c) Raman shift *vs* temperature for LO and TO modes in nano c-BN.
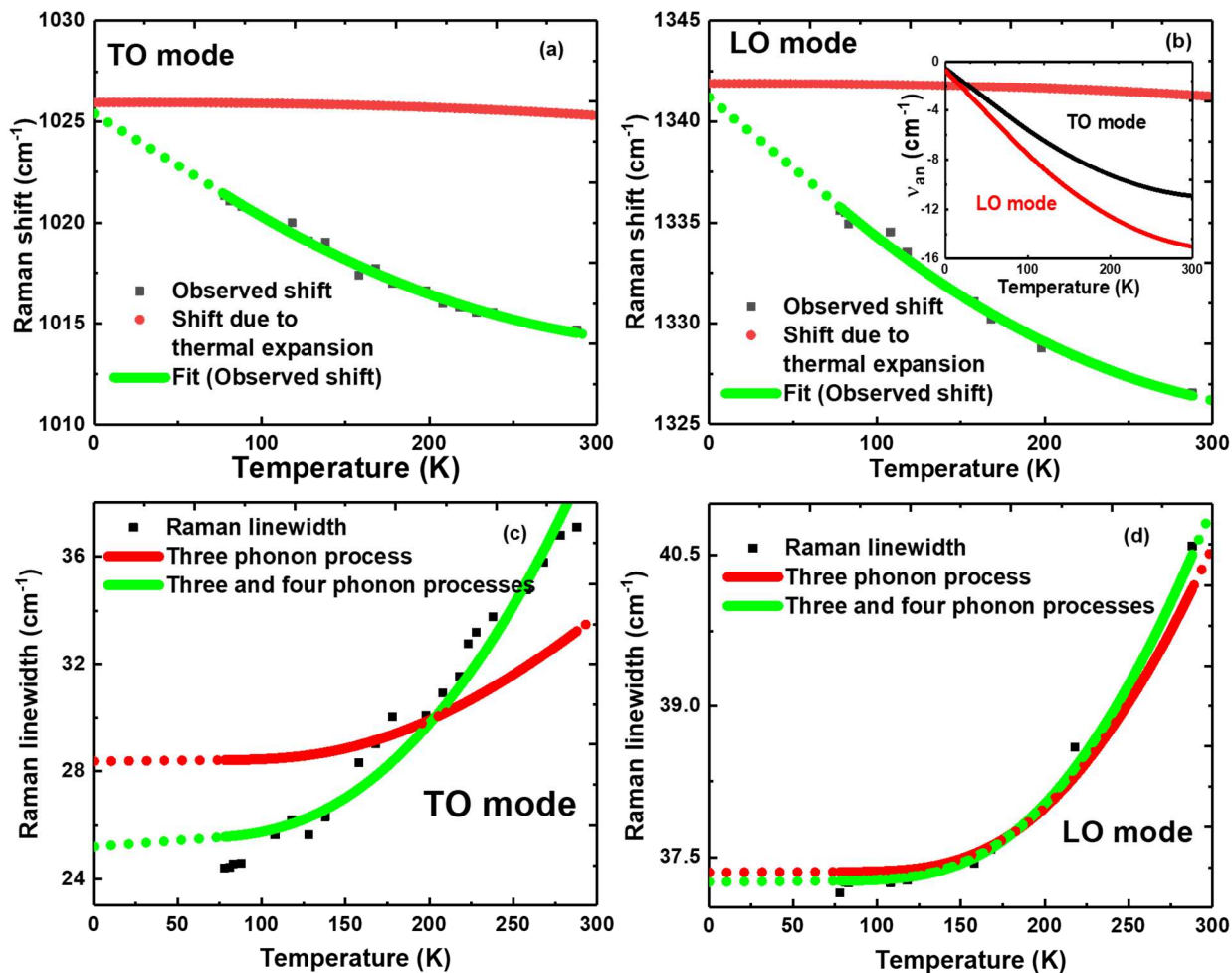
Figure 7: Temperature-dependent Raman analysis for nano c-BN: (a) Raman shift *vs* temperature for TO vibrational mode along with the shift due to thermal expansion, (b) Raman shift *vs* temperature for LO vibrational mode along with the shift due to thermal expansion with the inset showing the anharmonic shift *vs* temperature for TO and LO modes, (c) Raman linewidth *vs* temperature for TO mode showing the prominent presence of three and four phonon processes, and (d) Raman linewidth *vs* temperature for LO mode showing the prominent presence of three and four phonon processes.
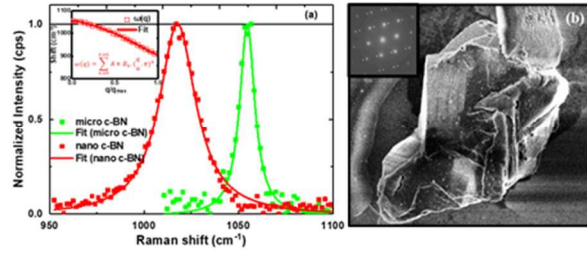
The controlled growth of phase-pure nano and microstructures of twinned c-BN will have tremendous impact on electrical and mechanical devices.